Interleaved signal multiplexing readout in depth encoding Prism-PET detectors

Yixin Li[1], **Andy LaBella**[2], **Xinjie Zeng**[1], **Zipai Wang**[3], **Eric Petersen**[3], **Xinjie Cao**[1], **Wei Zhao**[4], **Amir H. Goldan**[5,*]

[1]Department of Electrical and Computer Engineering, College of Engineering and Applied Sciences, Stony Brook University, Stony Brook, NY, US

[2]Department of Radiology, Boston Children's Hospital, Boston, MA, US

[3]Department of Biomedical Engineering, College of Engineering and Applied Sciences, Stony Brook University, Stony Brook, NY, US

[4]Department of Radiology, Renaissance School of Medicine, Stony Brook University, Stony Brook, NY, US

[5]Department of Radiology, Weill Cornell Medical College, Cornell University, New York, NY, US

Abstract

Background: Given the large number of readout pixels in clinical positron emission tomography (PET) scanners, signal multiplexing is an indispensable feature to reduce scanner complexity, power consumption, heat output, and cost.

Purpose: In this paper, we introduce interleaved multiplexing (iMux) scheme that utilizes the characteristic light-sharing pattern of depth-encoding Prism-PET detector modules with single-ended readout.

Methods: The iMux scheme shorts anodes from the four nearest neighbor silicon photomultiplier (SiPM) pixels that overlap with distinct light guides and connect to the same application-specific integrated circuit (ASIC) channel. The 4-to-1 coupled Prism-PET detector module was used which consisted of a 16×16 array of $1.5 \times 1.5 \times 20$ mm^3 lutetium yttrium oxyorthosilicate (LYSO) scintillator crystals coupled to an 8×8 array with 3×3 mm^2 SiPM pixels. A deep learning-based demultiplexing model was investigated to recover the encoded energy signals. Two different experiments were performed with non-multiplexed and multiplexed readouts to evaluate the spatial, depth of interaction (DOI), and timing resolutions of our proposed iMux scheme.

Results: The measured flood histograms, using the decoded energy signals from our deep learning-based demultiplexing architecture, achieved perfect crystal identification of events, and results were highly consistent with the non-multiplexed energy signals. The average energy, DOI

*****Correspondence** 525 East 68th Street, New York, NY 10065 amg4017@med.cornell.edu.
Yixin Li and Andy LaBella should be considered joint first authors.

and timing resolutions were $9.6 \pm 1.5\%$, 2.9 ± 0.9 mm, and 266 ± 19 ps for non-multiplexed readout and $10.3 \pm 1.6\%$, 2.8 ± 0.8 mm, and 311 ± 28 ps for multiplexed readout, respectively.

Conclusions: Our proposed iMux scheme improves on the already cost-effective and high-resolution Prism-PET detector module and provides 16-to-1 crystal-to-readout multiplexing without appreciable performance degradation. Also, only 4 SiPM pixels are shorted together in the 8×8 array to achieve 4-to-1 pixel-to-readout multiplexing, resulting in lower capacitance per multiplexed channel.

Keywords

deep learning; demultiplexing; Prism-PET; signal multiplexing

1 INTRODUCTION

Ultra-high resolution positron emission tomography (PET) imaging systems require an extremely large number of readout channels that increase scanner complexity, power consumption, heat output, and cost [1]. One method to overcome these challenges is to reduce the number of application-specific integrated circuit (ASIC) readout channels by multiplexing the silicon photo-multipliers (SiPM) pixels while minimizing performance degradations [2]. Various multiplexing methods have been proposed previously by other research groups where signals across multiple photodetectors are collected into a single readout channel [3–10]. The discretized positioning circuits (DPCs) [11–13] are used to implement charge division networks and require fewer passive electronic components than Anger logic [14]. However, undesirable resistive-capacitive (RC) delay from each SiPM degrades timing resolution [4]. The row-column summing method is another common design for multiplexing that can mitigate crosstalk between SiPM pixels but requires more preamplifiers and readout channels than DPC [15,16]. The symmetric charge division (SCD) network is a hybrid method that combines the design of a row-column summing readout circuit with the resistive chain but the large reduction in the number of readout channels comes with the trade-off of increased complexity for the readout circuit and reduced count-rate [17]. Finally, compared with resistive multiplexing design, the capacitive schemes improve the timing resolution but are more temperature sensitive and costly [18].

Previously, we designed a novel single-ended readout depth-encoding PET detector module with a segmented prismatoid light guide array, called the Prism-PET [19–21]. In this study, we introduce a new 4-to-1 pixel-to-ASIC multiplexing scheme that leverages the characteristic light-sharing pattern of the Prism-PET detector module. Moreover, we introduce a data-driven model for demultiplexing to recover the energy signal from all individual SiPM pixels. The flood histogram, energy, depth of interaction (DOI) and timing resolutions were measured for evaluating the performance of the non-multiplexed and multiplexed readout.

2 METHODS

Section 2.1 presents the formulas we used for positioning the gamma-ray interaction events in a 2D histogram and localizing the DOI value in a scintillation crystal. In section 2.2,

we present the scheme of our customized multiplexing board. Section 2.3 describes the methods for illustrating the spatial, DOI, and timing performance of the detector module when using our multiplexing scheme. Finally, we propose the CNN-based demultiplexing model in section 2.4.

2.1 Crystal identification and DOI encoding

Coincident events' position encoding in a light-sharing PET module with non-multiplexed readouts is performed using the weighted average energy method [22]

$$u = \frac{1}{P} \sum_{i=1}^{N} p_i x_i,$$

(1)

$$v = \frac{1}{P} \sum_{i=1}^{N} p_i y_i,$$

(2)

$$P = \sum_{i=1}^{N} p_i,$$

(3)

where (u, v) are the relative coordinates on the flood histogram, x_i and y_i is the x- and y-positions of the ith readout pixel in the detector, p_i is the light signal readout by the ith pixel, N is the total number of pixels in the readout array, and P is the sum of the signals collected by all pixels for a single gamma ray interaction event. DOI estimation was performed using the peak-to-total light energy ratio

$$w = \frac{p_{max}}{P},$$

(4)

where w is the DOI estimation parameter, p_{max} is the maximum light signal readout by a single pixel (i.e., the "primary" pixel), and P is the sum of light signal collected by all pixels (the same as Eq. 3). Unlike the uniform glass light guide design, Prism-PET utilizes a segmented light-guide array for localized light sharing across the nearest neighboring pixels and achieves a characteristic light-sharing pattern with enhanced crystal identification and DOI localization. Note that the scintillation photons are all contained within each optically isolated prismatoid mirror. Therefore, the denominator of Eq. 4 can be changed from P (total pixels signals) to the sum of only the N_p highest signals from the SiPM pixels sharing the same prismatoid mirrors

$$w = \frac{p_{max}}{\sum_{i=1}^{N_p} p_i},$$

(5)

where $N_p = 2, 3$, and 4 for edge, corner, and center crystals, respectively.

2.2 Multiplexing scheme design

The proposed interleaving multiplexing (iMux) scheme can be seen in Figure 1 where signals from the four nearest neighbor SiPM pixels that overlap with distinct prismatoid mirrors are shorted together and connect to the same ASIC channel, while SiPM pixels that overlap with the same prismatoid mirrors are connected to distinct ASIC channels.

For instance, we assume that gamma-ray interaction occurs on the primary crystal shown with a star (Figure 1) and is coupled to pixel 20. The four multiplexed ASIC channels with the highest signals are Mux 3, Mux 4, Mux 12 and Mux 13. Given our localized light sharing among horizontal, vertical, and diagonal nearest neighboring SiPMs (shown with arrows), our proposed iMux scheme will preserve the spatial information during signal encoding and mitigates any degradation in the crystal identification.

$$m = M \times s,$$

(6)

where m is a 16 by 1 vector representing the encoded readout signals and s is a 64 by 1 vector denoting the full SiPM pixel values for each interaction event. The 16 by 64 binary matrix M describes the multiplexing network that maps all 64 pixels to 16 encoded readout channels and is given as

$$M = \begin{bmatrix} 1\ 0\ 1 & & 0\ 0\ 0 \\ 0\ 0\ 0 & \cdots & 0\ 0\ 0 \\ 0\ 0\ 0 & & 0\ 0\ 0 \\ \vdots & \ddots & \vdots \\ 0\ 0\ 0 & & 0\ 0\ 0 \\ 0\ 0\ 0 & \cdots & 0\ 1\ 0 \\ 0\ 0\ 0 & & 0\ 0\ 0 \end{bmatrix},$$

(7)

where 4 positions are set to unity in each row and others are 0s given that each encoded readout channel signal is a sum of four SiPM pixels.

We artificially generated the 16 channels (16-ch) *synthetic* iMux readout data from the full 64 channels (64-ch) SiPM signals using Eq. 6 and regarded them as the ***training dataset*** for our deep learning model.

2.3 Experimental design and data acquisition

2.3.1 Prism-PET detector modules—We fabricated and acquired PET-like data on a 4-to-1 coupled Prism-PET detector module, where 4 crystals were optically coupled to 1 SiPM pixel. The module consisted of LYSO crystals (X-Lum, Shanghai, China) coupled to an 8×8 array of 3×3 mm^2 SiPM readout pixels (3.2 mm pitch, Hamamatsu S13361–3050AE-08) on one end and a prismatoid light guide on the opposite end, hence the name "Prism-PET". The LYSO crystal array for the 4-to-1 coupled Prism-PET module consists of a 16×16 array of $1.5 \times 1.5 \times 20$ mm^3 crystals (1.6 mm pitch). Prism-PET light guides were fabricated using SF10 glass with n = 1.767 and coupled to scintillator arrays using N0A170 adhesive with n = 1.7. Barium sulfate ($BaSO_4$), a material with diffusion reflection characteristics, was inserted between crystals (0.1 mm thickness), and throughout the top surface of the light guide to ensure the optical isolation of each prismatoid mirror. Additional information on the Prism-PET detector module can be found in the literature [19–21].

2.3.2 Point source experiment—Standard flood data acquisition was performed on the Prism-PET modules by uniformly exposing them with a 3 MBq Na-22 point source (1 mm active diameter) placed 15 cm away which is the minimum source-to-detector distance that maximizes the solid-angle coverage while minimizing performance degradation for edge and corner crystals (Fig.S-1 and Fig.S-2) due to oblique line of responses (LORs). Data readout was performed using a FEB/D_v2 readout board and time-of-flight (TOF) front-end-module (FEM) boards which comprising of TOFPET2 ASICs from PETsys Electronics. The experiment was performed inside the Espec BTU-133 benchtop test chamber set to a stable temperature of 15 °C [23].

In this experiment, datasets with and without multiplexing were acquired. Note that the dataset without multiplexing was labeled as the ground truth and used for training the deep learning model (Figure 2A). The experimental setup (Figure 2B) for multiplexing was implemented by interfacing the iMux board between the PETsys FEM256 board and the Prism-PET detector module.

2.3.3 DOI resolution calculation—The DOI estimation parameter w (Eq. 5) for each crystal was measured in singles mode from the point source experiment. The rising and falling edges of the w histogram as a pair of the error functions with the mean of the Gaussian derivatives assigned to 0 mm and 20 mm DOI values, respectively, were modeled to guide the linear mapping between w and DOI. The depth at 0 mm is assigned to the top interface which is coupled to the prismatoid light guide and the depth at 20 mm is assigned to the bottom interface which is coupled to the SiPM pixel. The crystal's DOI resolution was represented by the full width at half maximum (FWHM) of the fitted Gaussian function of the derivative of the w histogram's rising edge [24].

2.3.4 Timing experiment—A Na-22 source was placed in the middle of two opposing Prism-PET detector modules spaced a distance of 30 cm apart. Two coincidence experiments were performed without and with multiplexed readout and the timing resolution of LORs from two coincidence crystals was analyzed. The acquired list-mode data

was post-processed to filter for photopeak, inter-crystal scatter (ICS) events, and DOI (selecting coincidence events from the w histogram's rising edge) [25]. Benefiting from a characteristic pattern of SiPM signals in Prism-PET, the primary coincidence timestamps were corrected using the nearest-neighbor light-sharing timestamps (LSTS). A fine-tuning step was implemented using the LOR-based timing offset correction to further improve the timing resolution [24]. The measured timing spectra with different filters were fitted into Gaussian functions with their FWHM values representing the different coincidence timing resolutions (CTRs).

2.4   Signal demultiplexing

Although multiplexing signals from SiPM pixels to ASIC channels can be easily achieved by shorting the routes on the printed circuit board (PCB), the demultiplexing process has proven to be extremely challenging hard to estimate the original 64-channel data because the inverse process must solve an underdetermined system without a unique solution. In this work, we proposed a demultiplexing method based on a trained convolutional neural network (CNN) which uses 16-ch synthetic iMux and 64-ch ground-truth data.

In order to build a more accurate and faster demultiplexing architecture that can generalize to all Prism-PET detector modules, we considered the CNN architecture shown in Figure 3 which was implemented in Keras with Tensorflow as a backend on an NVIDIA Geforce RTX 3090 GPU. Based on the traditional U-net model [26], we simplified the architecture by reducing the number of kernels of each convolutional layer and the number of layers in both the contracting and expansive paths symmetrically. The multiplexed 16-ch data were reshaped to a 4×4 square matrix with the dimension of the output layer being an 8×8 square matrix to represent the original 64-ch demultiplexed data that was equal to the number of pixels in a SiPM detector module. The 2D convolutional layers in our CNN model used 2×2 kernels with 1 stride and each layer was followed by a rectified linear unit (ReLU) activation function. The weights in this network were initialized by the "He Normal Initialization" method which draws samples from a truncated normal distribution $N\left(0, \sqrt{2/n_{in}}\right)$, where n_{in} is the number of input units in the weight tensor [27]. Furthermore, the contracting and expansive paths included 2×2 MaxPooling and UpSampling layers, respectively, to accomplish feature downsampling and upsampling. The concatenation layers were utilized to connect the correspondingly cropped feature map from the contracting path to the expansive path.

During the training process, the predicted demultiplexed signals $\hat{s}$ are given as

$$\hat{s} = f(\boldsymbol{\theta} \mid \boldsymbol{m}),$$

(8)

where f represents the convolutional neural network, $\boldsymbol{\theta}$ denotes the uncertainty parameters of the model, and $\boldsymbol{m}$ is the multiplexed signals. We trained the neural network to find the optimal demultiplexing solution by minimizing the loss function of the predicted results and ground truth SiPM signals s. The network parameters $\boldsymbol{\theta}$ were iteratively updated during each

epoch to minimize the L2 squared norm loss function with the Adam stochastic optimization method [28]

$$\hat{\boldsymbol{\theta}} = \underset{\boldsymbol{\theta}}{\operatorname{argmin}} \| \boldsymbol{s} - \hat{\boldsymbol{s}} \|_2^2 .$$

(9)

For the training dataset, we collected around 350 million single events without using the iMux board (Figure 2A) and labeled them as the ground truth data, and generated the synthetic 16-ch iMux data (Eq. 6) as the training data for optimizing parameters of the model. Around 245 million events (70%) among the total data were used as training sets, and around 105 million events (30%) were validation sets. After the CNN was trained with the synthetic iMux data, the model was implemented for demultiplexing experimental signals (around 80 million events) from the iMux board (Figure 2B).

3 RESULTS

In section 3.1, we present experimental results of ground truth, multiplexed, and demultiplexed flood histograms. Sections 3.2 and 3.3 demonstrate the energy and DOI histograms for a few representative crystals, then summarize the energy and DOI resolutions for all crystals. Finally, the timing performance is shown in section 3.4.

3.1 Flood histogram and crystal identification

We plotted the flood histograms for a Prism-PET detector module in Figure 4. Excellent crystal separation was achieved in center, edge, and corner crystals for the non-multiplexed readout (Figure 4A). The floodmap (Figure 4B) for the synthetically multiplexed data showed the deteriorating effect of our proposed iMux scheme on crystal identification. However, our CNN-based demultiplexing technique successfully recovered signals in the correct floodmap and achieved excellent crystal separation in center, edge and corner crystals (Figure 4C). Figure 4D illustrated our trained CNN architecture was able to successfully demultiplex each event, which was from the actual multiplexed data using the iMux board (Figure 4E) that showed a similar pattern as Figure 4B, into a 64-ch energy frame and achieve excellent crystal separation in center, edge and corner crystals. Figure 4F and 4G showed line profiles for the central rows of Figure 4A and 4D demonstrating perfect crystal identification throughout the entire array without and with multiplexing with average peak-to-valley ratios of 5.2 and 4.9, respectively.

3.2 Energy performance

Figure 5A showed the Na-22 energy spectra without and with multiplexing for the 3 representative crystals located at the center, edge, and corner regions of the detector module. Figure 5B demonstrated the energy resolutions of all crystals. For the non-multiplexed readout, the energy resolution was $9.0 \pm 0.8\%$, $11.2 \pm 1.1\%$, and $12.3 \pm 2.2\%$ for center, edge, and corner crystals, respectively, with a mean energy resolution of $9.6 \pm 1.5\%$. In terms of the multiplexed readout, the energy resolution was $9.8 \pm 0.9\%$, $11.9 \pm 1.7\%$,

and 12.4 ± 2.9% for center, edge, and corner crystals, respectively, with a mean energy resolution being 10.3 ± 1.6%.

3.3 DOI performance

Figure 6A demonstrated the DOI estimation parameter w histograms of Na-22 without and with multiplexing for the 3 representative crystals located at the center, edge, and corner regions of the detector module. Figure 6B showed the DOI resolutions of all crystals. For the non-multiplexed readout, the DOI resolution was 2.8 ± 0.8 mm, 3.1 ± 1.1 mm, and 3.2 ± 0.9 mm FWHM for center, edge, and corner crystals, respectively, with a mean DOI resolution being 2.9 ± 0.9 mm. In terms of multiplexed readout, the DOI resolution was 2.6 ± 0.7 mm, 3.1 ± 0.9 mm, and 3.2 ± 0.8 mm FWHM for center, edge, and corner crystals, respectively, with a mean DOI resolution of 2.8 ± 0.8 mm.

3.4 Timing performance

Figure 7 shows the TOF histograms with the non-multiplexed and multiplexed readout. The list-mode data was processed to filter ICS events in the photopeak. The average CTR of non-multiplexed readout was 266 ± 19 ps FWHM across all crystals after further corrections using DOI information, the nearest-neighbor LSTSs, and LOR-based fine-tuning [24]. The corresponding CTR with the iMux board readout was 311 ± 28 ps FWHM.

4 DISCUSSION

We have experimentally demonstrated the viability of our proposed multiplexing scheme which is based on the characteristic light-sharing pattern of the Prism-PET detector module. For the 8×8 SiPM array, iMux achieves the same SiPM-to-ASIC multiplexing ratio as the conventional row-column summing readout circuit but with half the capacitance and dark counts for each output channel due to interleaved shorting of anodes for only 4 SiPMs.

Moreover, the proposed data-driven demultiplexing model achieved perfect crystal identification without any additional decoding error. Compared with other classical or conventional machine learning techniques such as the look-up table or k-Nearest Neighbor (kNN), which are trained by simply memorizing the features and labels of the training dataset while requiring extensive computational resources during the prediction process [29], the CNN method spends most of the time on training the model to optimize parameters and learn generalizable representations which combined with GPU-based parallel processing can perform data demultiplexing substantially faster.

Measured energy histograms using both non-multiplexed and multiplexed readouts were identical in the photopeak energy window of 400–650 keV and although not significant, some deviations were seen for edge and corner crystals outside the energy window at the low energies. This is due to the smaller dynamic range of the charge-to-digital converter (QDC) assigned to edge and corner crystals during the PETsys calibration procedure and the limitation of CNN-based demultiplexing at very QDC values. Nevertheless, this limitation did not degrade the energy performance of the detector module with iMux readout and the average energy difference between non-multiplexed and multiplexed readouts was only 0.7% around the 511 keV photopeak.

The measured w histogram using both non-multiplexed and multiplexed readouts showed identical trends with a noticeable offset observed for corner crystals. One must note that the difficulty for energy demultiplexing increases from the center to edge, to corner crystals, and these w- offsets are due to a slightly higher weighting of CNN demultiplexed energies for the primary SiPMs when compared to those for the non-multiplexed readout. However, the w-offset will not deteriorate the DOI performance because the w histogram can be converted to DOI distribution through linear regression fitting [22] and the identical trend of the w histogram would result in the same DOI resolution. Therefore, we assert that the use of the iMux board will not make a noticeable degradation in DOI performance.

The discriminator threshold V_{th_t1} in the PETsys ASIC configuration is a parameter that directly affects the timing resolution [30,31] and has been optimized for iMux readout to improve the CTR (i.e., V_{th_t1} is set to 20 and 50 for non-multiplexed and multiplexed readouts, respectively). In the end, the timing resolution only degraded by ~17% using the iMux board as compared to the non-multiplexed readout. This expected degradation is due to the added capacitance of iMux readout channels when 4 interleaved SiPM anodes are shorted together. Another reason for the slightly worse timing resolution may be the extra connectors and cables required when using the iMux adapter board. In the future, our proposed iMux scheme will be implemented directly on the SiPM board which will then connect directly to the ASIC readout using one short flexible cable and this is expected to improve the timing performance. Finally, the overvoltage of PETsys SiPM bias setting is another parameter that can affect the timing resolution and needs to be optimized for iMux readout. [31]

5 CONCLUSION

In this research, we have developed an interleaving connection scheme of SiPM anodes for signal multiplexing based on the characteristic light-sharing pattern of our cost-effective and high-resolution Prism-PET detector modules with single-ended depth encoding readout. We also showed highly accurate CNN-based signal demultiplexing without noticeable degradation in spatial, energy, DOI, and timing resolutions when compared to the non-multiplexed readout. Our proposed multiplexing scheme enhances Prism-PET's commercial viability, power efficiency, and cost-effectiveness.

Supplementary Material

Refer to Web version on PubMed Central for supplementary material.

References

[1]. Lee S, Choi Y, Kang J, and Jung JH, Development of a multiplexed readout with high position resolution for positron emission tomography, Nuclear Instruments and Methods in Physics Research Section A: Accelerators, Spectrometers, Detectors and Associated Equipment 850, 42–47 (2017).

[2]. Kim E, Hong KJ, Yeom JY, Olcott PD, and Levin CS, Trends of data path topologies for data acquisition systems in positron emission tomography, IEEE Transactions on Nuclear Science 60, 3746–3757 (2013).

[3]. Olcott PD, Habte F, Zhang J, and Levin CS, Charge multiplexing readout for position sensitive avalanche photodiodes, in IEEE Nuclear Science Symposium Conference Record, 2005, volume 5, pages 2935–2937, IEEE, 2005.

[4]. Goertzen AL et al. , Design and performance of a resistor multiplexing readout circuit for a SiPM detector, IEEE Transactions on Nuclear Science 60, 1541–1549 (2013).

[5]. Jung JH, Choi Y, Hong KJ, Hu W, Kang JH, Min BJ, Shin SH, Lim HK, Huh YS, and Kim E-J, Development of a position decoder circuit for PET consisting of GAPD arrays, Nuclear Instruments and Methods in Physics Research Section A: Accelerators, Spectrometers, Detectors and Associated Equipment 621, 310–315 (2010).

[6]. Bieniosek M, Cates J, and Levin C, Achieving fast timing performance with multiplexed SiPMs, Physics in Medicine & Biology 61, 2879 (2016). [PubMed: 26987898]

[7]. Kwon I, Kang T, and Hammig MD, Experimental validation of charge-sensitive amplifier configuration that compensates for detector capacitance, IEEE Transactions on Nuclear Science 63,1202–1208 (2016).

[8]. Bieniosek MF, Cates J, Grant A, and Levin CS, Analog filtering methods improve leading edge timing performance of multiplexed SiPMs, Physics in Medicine & Biology 61, N427 (2016). [PubMed: 27484131]

[9]. Seo M, Park H, and Lee JS, Evaluation of large-area silicon photomultiplier arrays for positron emission tomography systems, Electronics 10, 698 (2021).

[10]. Xu T, Wang S, Wei Q, Liu W, Gong G, Deng Z, Ma T, and Liu Y, Development of multi-channel fast SiPM readout electronics for clinical TOF PET detector, in 2014 Ieee Nuclear Science Symposium and Medical Imaging Conference (Nss/Mic), pages 1–3, IEEE, 2014.

[11]. Jeon S-J, Kim J, Ji M-G, Park J-H, and Choi Y-W, Position error correction using homography in discretized positioning circuit for gamma-ray imaging detection system, IEEE Transactions on Nuclear Science 64, 816–819 (2016).

[12]. Zhang X-H, Qi Y-J, and Zhao C-L, Design and development of compact readout electronics with silicon photomultiplier array for a compact imaging detector, Chinese Physics C 36, 973 (2012).

[13]. Liu C-Y and Goertzen AL, Multiplexing approaches for a 12×4 array of silicon photomultipliers, IEEE Transactions on Nuclear Science 61, 35–43 (2013).

[14]. Anger HO, Scintillation camera, Review of scientific instruments 29, 27–33 (1958).

[15]. Stratos D, Maria G, Eleftherios F, and George L, Comparison of three resistor network division circuits for the readout of 4× 4 pixel SiPM arrays, Nuclear Instruments and Methods in Physics Research Section A: Accelerators, Spectrometers, Detectors and Associated Equipment 702, 121–125 (2013).

[16]. Kwon SI and Lee JS, Signal encoding method for a time-of-flight PET detector using a silicon photomultiplier array, Nuclear Instruments and Methods in Physics Research Section A: Accelerators, Spectrometers, Detectors and Associated Equipment 761, 39–45 (2014).

[17]. Olcott PD, Talcott JA, Levin CS, Habte F, and Foudray AM, Compact readout electronics for position sensitive photomultiplier tubes, IEEE Transactions on Nuclear Science 52, 21–27 (2005).

[18]. Yang Q, Kuang Z, Sang Z, Yang Y, and Du J, Performance comparison of two signal multiplexing readouts for SiPM-based pet detector, Physics in Medicine & Biology 64, 23NT02 (2019).

[19]. LaBella A, Zhao W, Lubinsky R, and Goldan AH, Prismatoid light guide array for enhanced gamma ray localization in PET: a Monte Carlo simulation study of scintillation photon transport, Physics in Medicine & Biology 65, 18LT01 (2020).

[20]. LaBella A, Cao X, Petersen E, Lubinsky R, Biegon A, Zhao W, and Goldan AH, High-resolution depth-encoding PET detector module with prismatoid light-guide array, Journal of Nuclear Medicine 61, 1528–1533 (2020). [PubMed: 32111684]

[21]. LaBella A, Lubinsky R, Zhao W, and Goldan AH, Prism mirror light guide for enhanced gamma ray localization in PET, in 2019 IEEE Nuclear Science Symposium and Medical Imaging Conference (NSS/MIC), pages 1–4, IEEE, 2019.

[22]. Pizzichemi M, Stringhini G, Niknejad T, Liu Z, Lecoq P, Tavernier S, Varela J, Paganoni M, and Auffray E, A new method for depth of interaction determination in PET detectors, Physics in Medicine & Biology 61, 4679 (2016). [PubMed: 27245174]

[23]. Schug D, Nadig V, Weissler B, Gebhardt P, and Schulz V, Initial measurements with the PET-sys TOFPET2 ASIC evaluation kit and a characterization of the ASIC TDC, IEEE Transactions on Radiation and Plasma Medical Sciences 3, 444–453 (2018).

[24]. Zeng X et al. , A conformal TOF-DOI Prism-PET prototype scanner For high resolution quantitative neuroimaging, Medical physics.

[25]. Cao X, Labella A, Zeng X, Zhao W, and Goldan AH, Depth of interaction and coincidence time resolution characterization of ultrahigh resolution time-of-flight prism-PET modules, IEEE Transactions on Radiation and Plasma Medical Sciences 6, 529–536 (2021).

[26]. Ronneberger O, Fischer P, and Brox T, U-net: Convolutional networks for biomedical image segmentation, in Medical Image Computing and Computer-Assisted Intervention-MICCAI 2015: 18th International Conference, Munich, Germany, October 5–9, 2015, Proceedings, Part II118, pages 234–241, Springer, 2015.

[27]. He K, Zhang X, Ren S, and Sun J, Delving deep into rectifiers: Surpassing human-level performance on imagenet classification, in Proceedings of the IEEE international conference on computer vision, pages 1026–1034, 2015.

[28]. Kingma DP and Ba J, Adam: A method for stochastic optimization, arXiv preprint arXiv:1412.6980 (2014).

[29]. Liu W, Wei J, and Meng Q, Comparisions on KNN, SVM, BP and the CNN for Handwritten Digit Recognition, in 2020 IEEE International Conference on Advances in Electrical Engineering and Computer Applications (AEECA), pages 587–590, IEEE, 2020.

[30]. Yoshida E, Obata F, Kamada K, Yoshikawa A, and Yamaya T, Development of crosshair light sharing PET detector with TOF and DOI capabilities using fast LGSO scintillator, Physics in Medicine & Biology 66, 225003 (2021).

[31]. Nadig V, Schug D, Weissler B, and Schulz V, Evaluation of the PETsys TOFPET2 ASIC in multichannel coincidence experiments, EJNMMI physics 8, 1–21 (2021). [PubMed: 33409746]
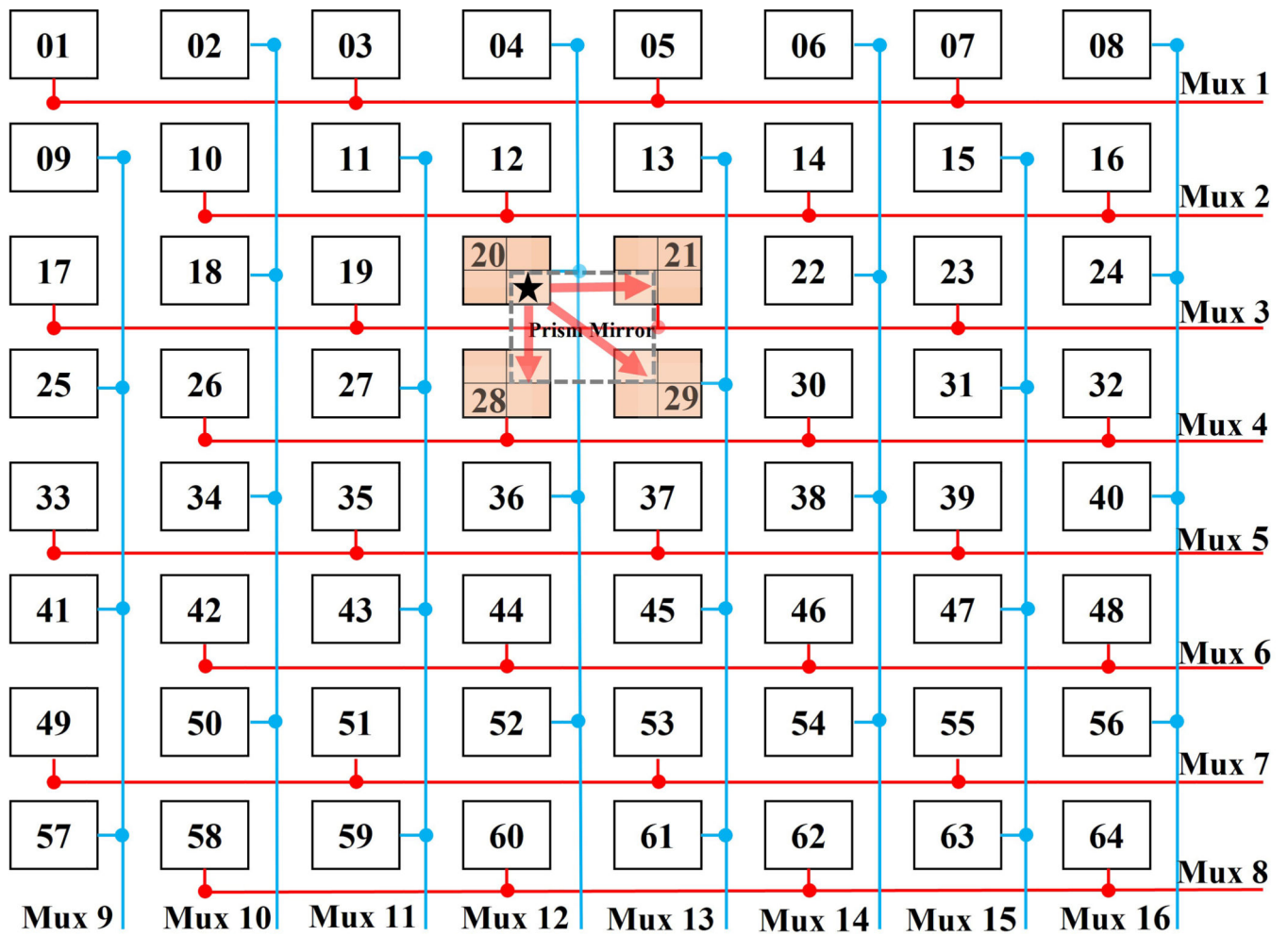
Figure 1.
Schematic of iMux. Square blocks are SiPM pixels. Red and blue lines are connecting patterns.
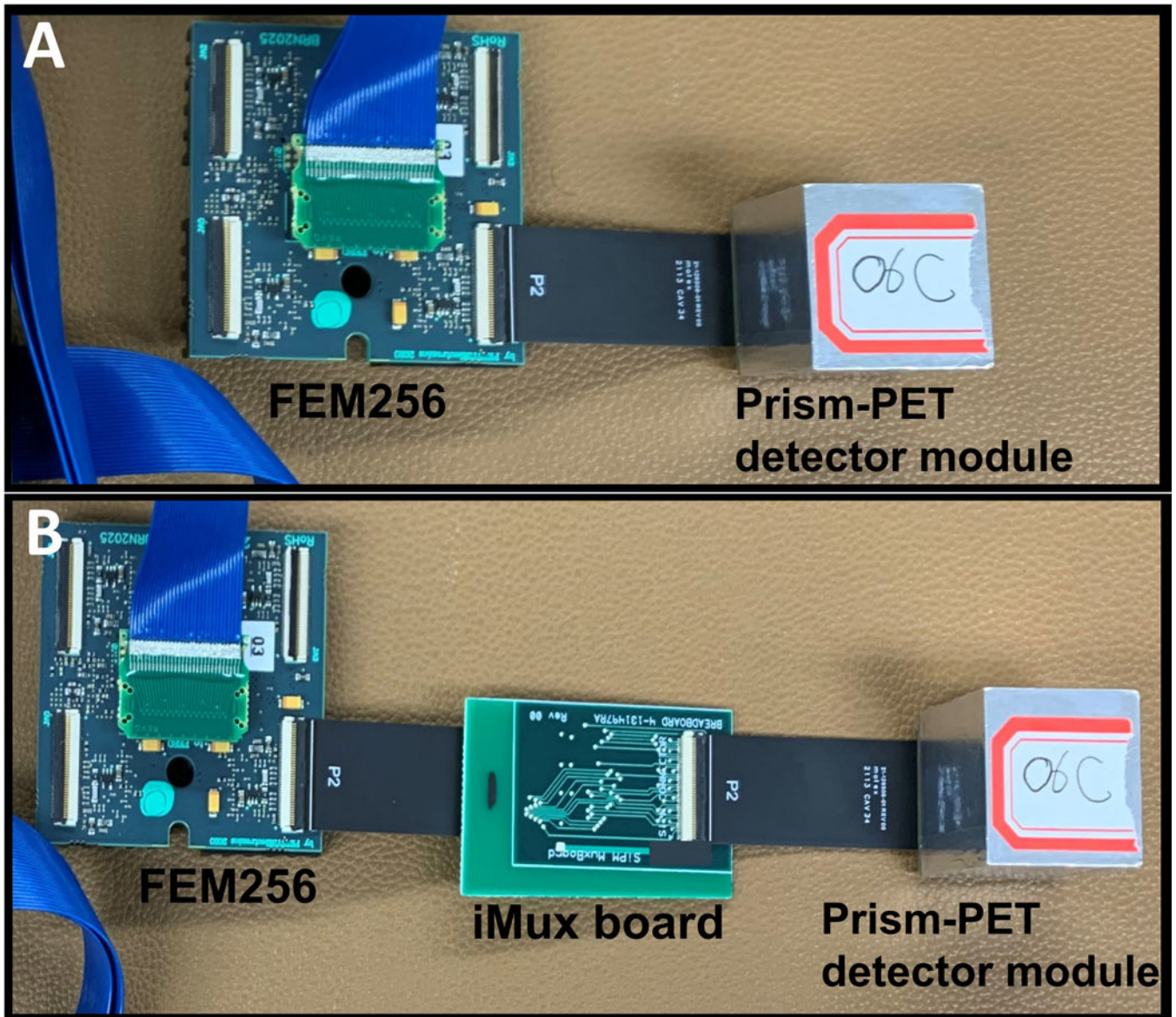
Figure 2.
(A) Image showing the direct connection between the FEM256 board and the Prism-PET module. (B) Image of the custom multiplexing readout board connected to the FEM256 board and the Prism-PET module.
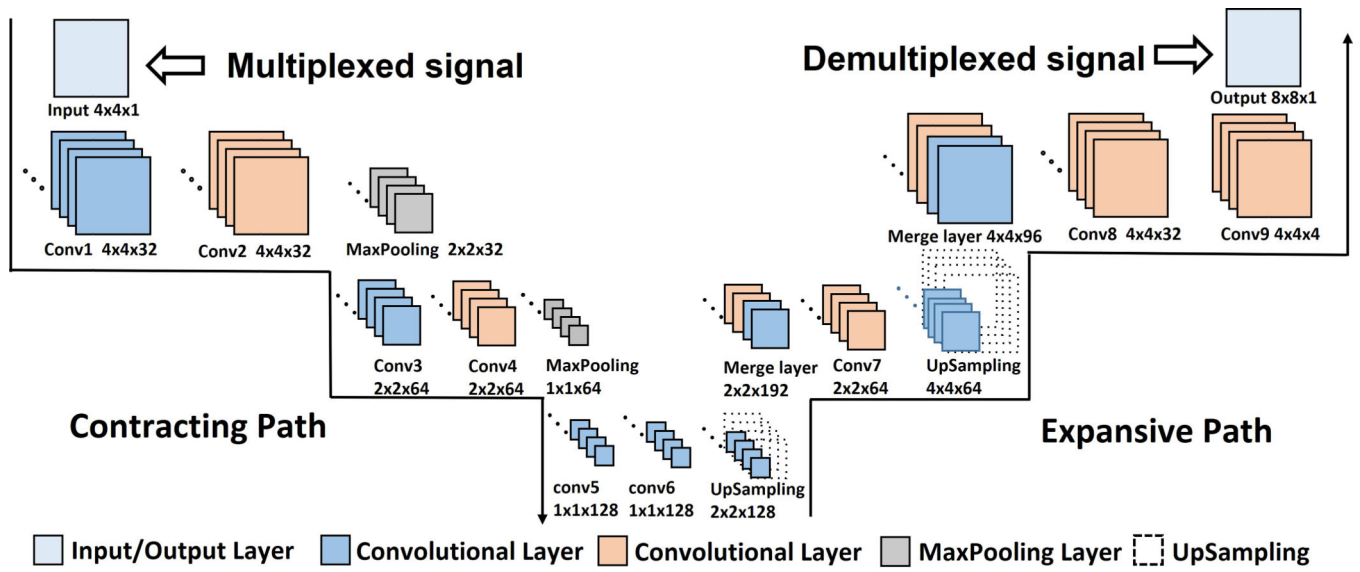
Figure 3.
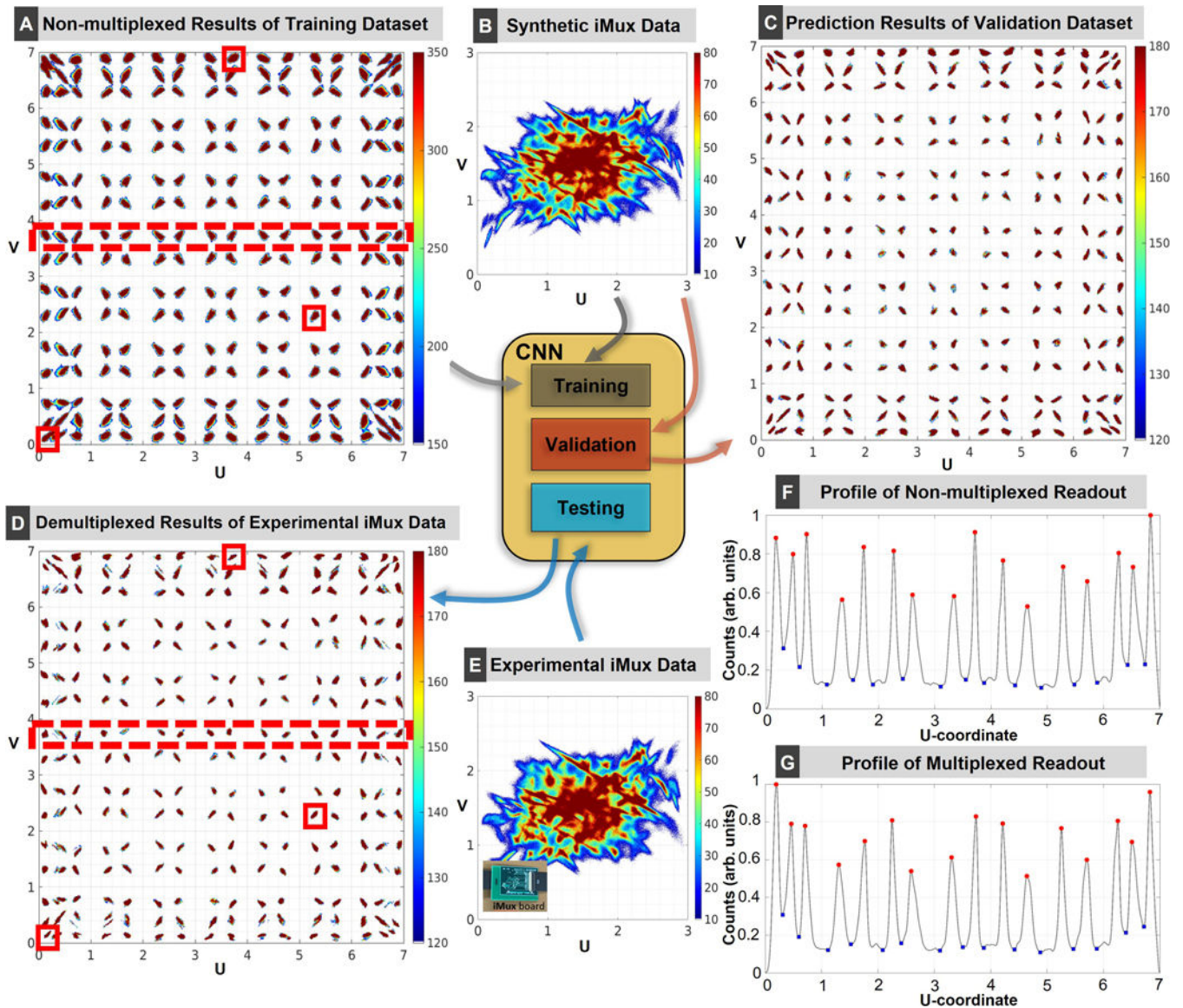Schematic of deep learning framework.

Figure 4.
Flood histogram results for the Prism-PET detector module following CNN-based demultiplexing. The central inset shows the dataset used for each stage in the CNN (the arrow pointing into the inset means the flood map was used for model training or testing, and the arrow pointing outward means the dataset was output by the CNN). The representative crystals were selected in red squares to perform the energy and DOI histograms in sections 3.2 and 3.3. (A) Flood map of the non-multiplexed 64-ch training dataset. (B) Flood map of synthetic multiplexed 16-ch data. (C) CNN demultiplexing results for the Prism-PET validation dataset. (D) CNN demultiplexing results for the iMux board experimental dataset. (E) Experimental multiplexed data acquired by the iMux board. (F) The profile of the central row of the crystals using non-multiplexed readout. (G) The profile of the central row of the crystals using multiplexed readout.
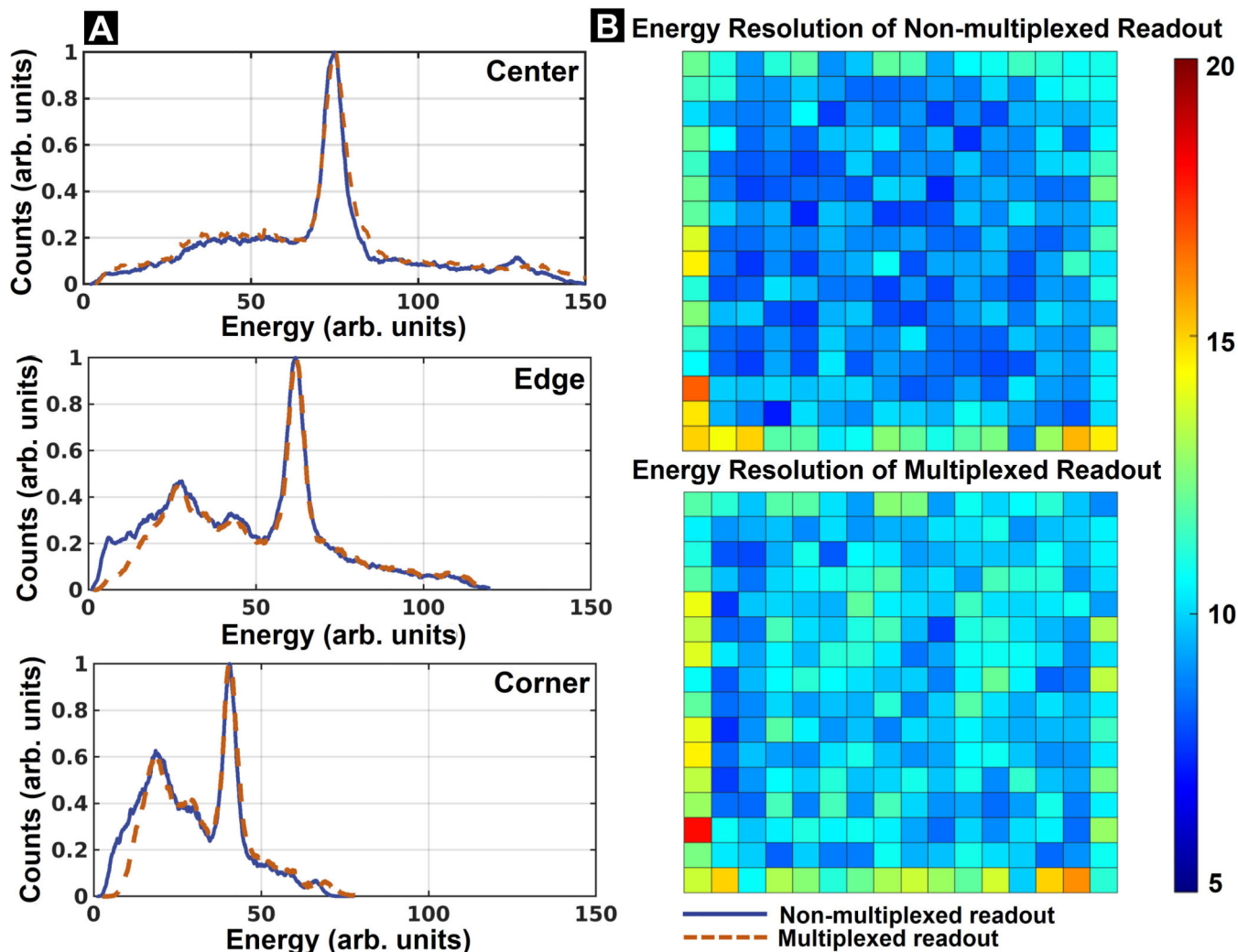
Figure 5.
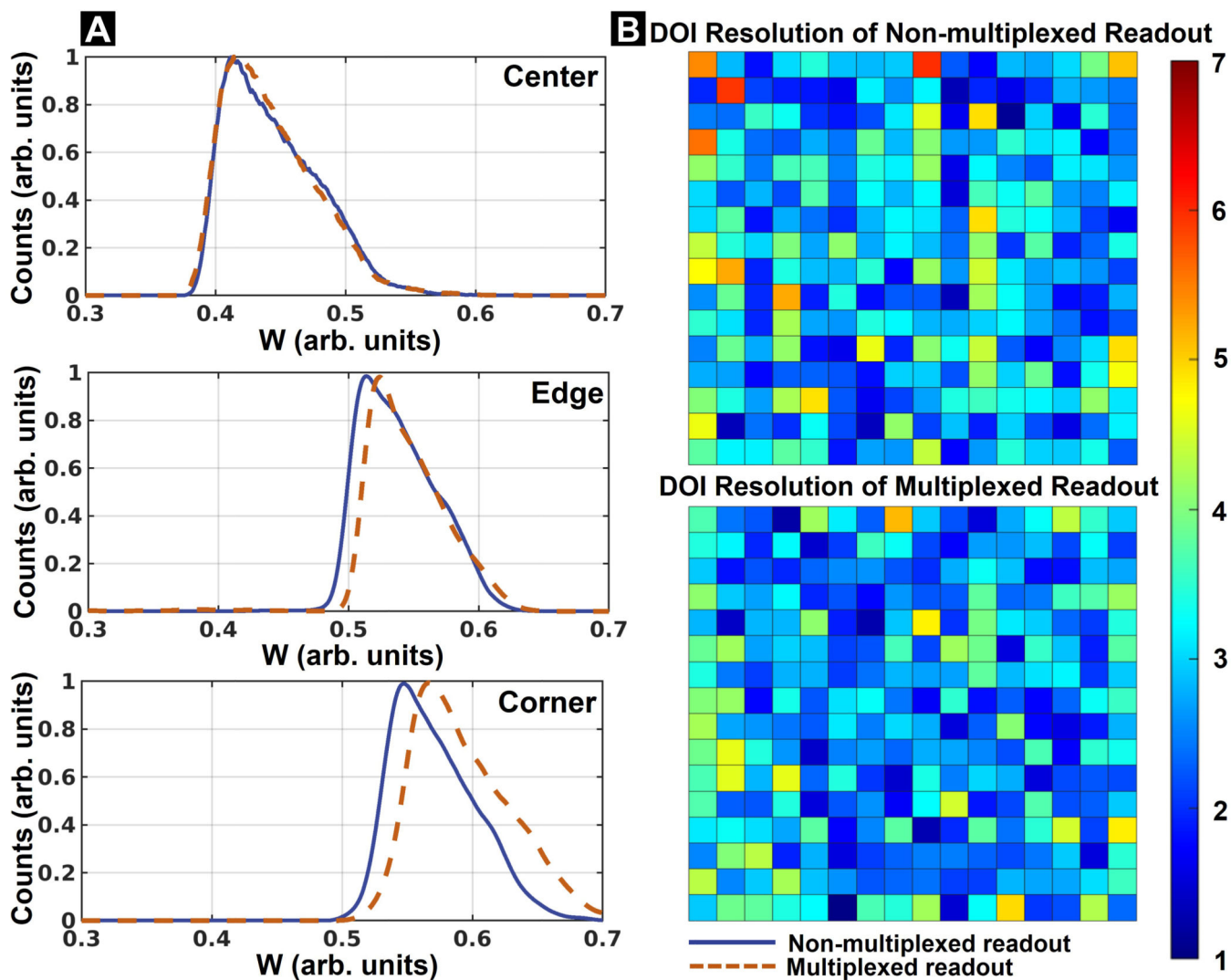(A) Energy histograms for center, edge, and corner crystals. Solid and dashed lines represent histograms for non-multiplexed and multiplexed readouts, respectively. (B) The 2D mapping of the energy resolutions of 256 individual LYSO crystals in the 16×16 array of a Prism-PET detector module without/with using iMux board.

Figure 6.
(A) w histograms for center, edge, and corner crystals. Solid and dashed lines represent histograms for non-multiplexed and multiplexed readouts, respectively. (B) The 2D mapping of the DOI resolutions of 256 individual LYSO crystals in the 16×16 array of a Prism-PET detector module without/with using iMux board.
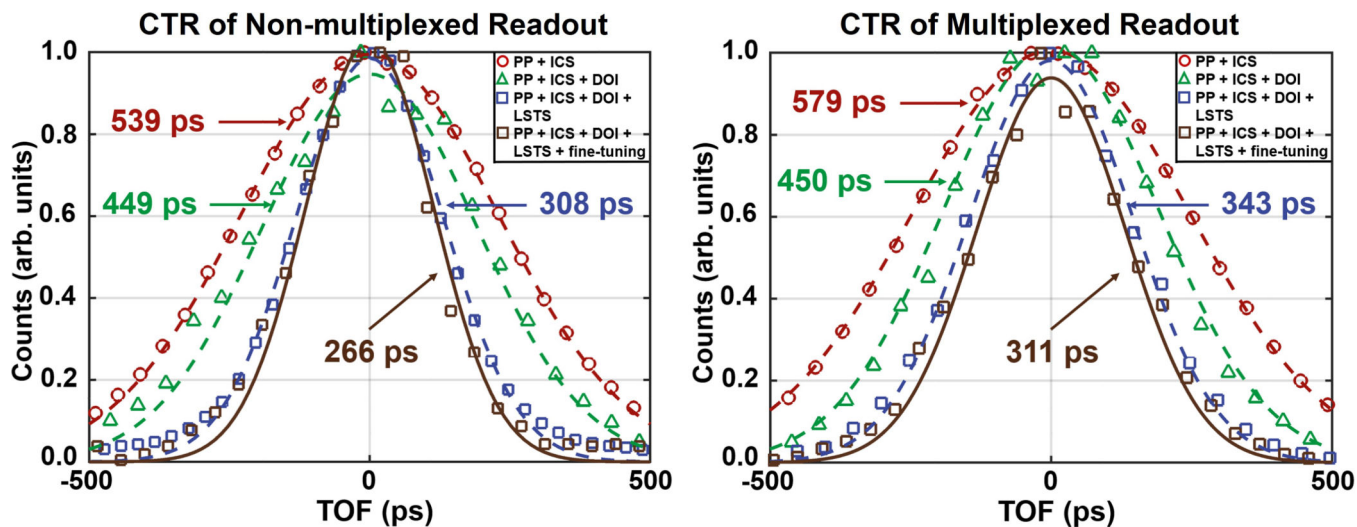
Figure 7.

TOF histograms of two coincidence detector modules without ($V_{th\_t1} = 20$) and with ($V_{th\_t1} = 50$) multiplexed readout using the following corrections of photopeak (PP) events: (1) filtered for ICS (red); (2) filtered for ICS and corrected using DOI information (green); (3) filtered for ICS and corrected using both DOI information and nearest-neighbor LSTSs (blue); (4) further filtered using LOR-based fine-tuning (brown).